

Giant enhancement of anomalous Hall effect in Cr modulation-doped non-collinear antiferromagnetic Mn₃Sn thin films

Xin Chen¹, Hang Xie¹, Qi Zhang^{1,2}, Ziyang Luo³, Lei Shen^{4,5}, and Yihong Wu^{1,6,*}

¹*Department of Electrical and Computer Engineering, National University of Singapore, Singapore 117583*

²*Department of Electrical and Electronic Engineering, Southern University of Science and Technology, Xueyuan Rd 1088, Shenzhen 518055, China*

³*School of Physics and Electronics, Central South University, Changsha 410083, China*

⁴*Department of Mechanical Engineering, National University of Singapore, Singapore 117575*

⁵*Engineering Science Programme, National University of Singapore, Singapore 117575*

⁶*National University of Singapore (Chong Qing) Research Institute, Chongqing Liang Jiang New Area, Chongqing 401123, China*

E-mail: elewuyh@nus.edu.sg

We report on Cr doping effect in Mn₃Sn polycrystalline films with both uniform and modulation doping. It is found that Cr doping with low concentration does not cause notable changes to the structural and magnetic properties of Mn₃Sn, but it significantly enhances the anomalous Hall conductivity, particularly for modulation-doped samples at low temperature. A Hall conductivity as high as 184.8 $\Omega^{-1} \text{ cm}^{-1}$ is obtained for modulation-doped samples at 50 K, in a sharp contrast to vanishingly small values for undoped samples at the same temperature. We attribute the enhancement to the change of Fermi level induced by Cr doping.

Recently Mn_3X ($X = Sn, Ge, Ga, Rh, Ir, Pt$) based non-collinear antiferromagnets (AFMs) have attracted significant attention¹⁻¹⁰⁾ because, unlike the widely studied collinear AFMs, these non-collinear AFMs exhibit large anomalous Hall,¹⁻⁴⁾ anomalous Nernst⁵⁾ and magneto-optical Kerr⁷⁾ effects at room temperature and importantly, all these effects are accessible via either a moderate Oersted field or an effective spin torque field.⁸⁻¹⁰⁾ It has also been shown that these non-collinear AFMs host a wide range of exotic phenomena from magnetic Weyl fermions,^{11,12)} to ferroic ordering of cluster octupole moment,¹³⁾ spin polarized current¹⁴⁾ and magnetic spin Hall effect.¹⁵⁾ These exciting findings suggest that the chiral spin structure and the resultant Berry curvature affect profoundly the charge and spin transport properties and make the Mn_3X -based AFMs not only appealing for fundamental studies but also promising for spintronics applications. For the latter, it is important to prepare Mn_3X thin films using commonly available deposition techniques such as sputtering, which has already been reported by several groups.¹⁶⁻²¹⁾ The initial results are encouraging as similar phenomena reported in bulk samples were also observed in thin films, albeit the size of the corresponding effect such as anomalous Hall effect (AHE) is typically much smaller than that of bulk samples, suggesting that further studies are required to improve the structural and physical properties of Mn_3X thin films.

As the distribution of the non-zero Berry curvature and their relative positions to the Fermi level play an important role in determining the transport properties of Mn_3X -based AFMs, one of the possible pathways is to tune the Fermi level by chemical doping without significantly affecting the electronic band structures. In this context, we investigate Cr-doping effect on the structural, magnetic, and transport properties of Mn_3Sn , a representative Mn_3X -based AFM, via both uniform and modulation doping. It is found that both doping techniques lead to a large enhancement of AHE below room temperature compared to undoped samples, particularly for the modulation-doped samples. In addition to AHE, we also observe an enhancement of negative magnetoresistance (MR) when the external magnetic field and current are parallel.

All the samples are deposited on SiO_2/Si substrates by magnetron sputtering at room temperature with a base pressure of 2×10^{-8} Torr and a working pressure of 3×10^{-3} Torr. Uniform doping is achieved through co-sputtering of Mn_3Sn and Cr with the Cr composition controlled by the sputtering powers of both targets. As for modulation-doped samples, we form $[Mn_3Sn(t_1)/Cr(t_2)]_N$ multilayers and use the individual layer thickness to control the equivalent Cr composition; here t_1 and t_2 are the thicknesses of Mn_3Sn and Cr in *nm* and N is the repetition

number. All the samples are post-annealed at 450°C in vacuum with a base pressure of 2×10^{-5} Torr for 1 hour to promote both crystallization and dopant diffusion. Crystalline structures of the samples are analyzed using X-ray diffraction (XRD) on a RIGAKU Smartlab system with Cu K α radiation. Magnetic measurements are performed using SQUID (Superconducting Quantum Interference Device) magnetometry. For AHE and MR measurements, the samples are patterned into Hall bars with a lateral dimension of 150 μm (length) \times 15 μm (width) using combined techniques of photolithography, sputtering and lift-off. The electrical measurements are performed in a Quantum Design's VersaLab system.

Figure 1 shows the XRD patterns of three groups of samples. The first group is a single layer Mn₃Sn (label it as MS below) with a thickness of 72 nm. The second group consists of three [Mn₃Sn(2.4)/Cr(t_2)]₃₀ samples with $t_2 = 0.15, 0.3$ and 0.6 nm, respectively. In the third group are two co-sputtered samples deposited at the same Mn₃Sn cathode power of 50 W, but with a different Cr cathode power of 10 W (MS50Cr10) and 30 W (MS50Cr30). The atomic compositions of Mn and Sn in Mn₃Sn analyzed by X-ray photoelectron spectroscopy (XPS) are 0.79 and 0.21, respectively, which are clearly Mn-rich compared to the stoichiometric composition. On the other hand, the equivalent atomic compositions of [Mn₃Sn(2.4)/Cr(0.3)]₃₀ and [Mn₃Sn(2.4)/Cr(0.6)]₃₀ are Mn: 0.6 and 0.49, Sn: 0.19 and 0.15, and Cr: 0.21 and 0.36, respectively. The XRD peaks for Mn₃Sn include $(10\bar{1}1)$, $(11\bar{2}0)$, $(20\bar{2}0)$, (0002) , $(20\bar{2}1)$, $(20\bar{2}2)$, $(22\bar{4}0)$, $(22\bar{4}2)$, and $(40\bar{4}1)$, indicating that it is polycrystalline with a mixture of crystallites with different orientations. The XRD peaks for [Mn₃Sn(2.4)/Cr(t_2)]₃₀ are more or less the same as that of Mn₃Sn except that the (0002) peak becomes smaller. On the other hand, the XRD patterns of the two co-sputtered samples are almost the same as that of the Mn₃Sn sample including the peak positions. The lattice constant a of Mn₃Sn is calculated to be 5.673 Å, while those of Cr-doped samples are all around 5.666 Å, close to that of bulk Mn₃Sn (~ 5.666 Å).²²⁾ We have also conducted low angle X-ray reflectometry (XRR) measurements for [Mn₃Sn(2.4)/Cr(t_2)]₃₀ with $t_2 = 0.3, 0.6, 0.9, 1.2$ and 1.8 nm, but we didn't observe any peak due to the periodicity of the multilayer except for the $t_2 = 1.8$ nm sample, which exhibits a very weak peak. The above XRD and XRR results suggest that both the uniform and modulation-doped Mn₃Sn exhibits similar crystalline structure as that of undoped samples, suggesting good solubility of Cr in Mn₃Sn in both cases.

Figures 2 (a) – (d) show the M - H curves of these samples measured at 300 K by applying the field in different directions, namely, out-of-plane (red solid-line), in-plane 0° (green dotted-line), in-plane 45° (purple dashed-line) and in-plane 90° (black dash dotted-line). Here, we take one side edge of the sample as the reference for the in-plane field, *i.e.*, in-plane 0° . The out-of-plane saturation magnetizations (M_s) of $[\text{Mn}_3\text{Sn}(2.4)/\text{Cr}(0.15)]_{30}$, $[\text{Mn}_3\text{Sn}(2.4)/\text{Cr}(0.6)]_{30}$, and MS50Cr10 at 300 K are 7.28, 9.04, 7.03, and 8.07 emu/cm³, respectively. These values are on the same order of the M_s reported for polycrystalline Mn_3Sn films at 300 K.^{20,23,24} The shape of both in-plane and out-of-plane M - H curves can be fitted well using the formula

$$M = \frac{2M_s}{\pi} \sum_{i=1}^n \alpha_i \text{atan}[\beta_i(H \pm H_{ci})], \quad (1)$$

where M_s is the total saturation magnetization, n is the number of a particular type of crystallites with a distinctive crystalline orientation, α_i is a proportional coefficient to denote the contribution from crystallites with different orientations with $\sum_{i=1}^n \alpha_i = 1$, β_i indicates the projection of external field on the c -plane, and H_{ci} is the coercivity when the field is applied in plane. The “ \pm ” sign indicates the forward and backward sweeping curves, respectively. We find that all the M - H curves can be fitted reasonably well with $n = 3$. The fitting results (Figures S1 and S2 in supplementary data) suggest that the combined contribution from $(11\bar{2}0)$, $(20\bar{2}0)$ and $(22\bar{4}0)$ planes to the out-of-plane magnetization of Mn_3Sn is about 35%, the other 50% is due to $(20\bar{2}1)$ and $(40\bar{4}1)$ planes, and the remaining 15% goes to $(10\bar{1}1)$ and $(20\bar{2}2)$ planes. For $[\text{Mn}_3\text{Sn}(2.4)/\text{Cr}(0.15)]_{30}$ the same ratios are 25%, 55% and 20%, respectively, indicating a slight change in the crystallite orientations. The results are consistent with the intensity ratio of XRD peaks. Figure 2(e) shows the temperature-dependence of M_s for the four samples measured at 200 Oe during the warming up sweep after the sample is zero-field cooled to 50 K. As can be seen, the magnetization of Mn_3Sn decreases monotonically from 300 K to 250 K and becomes almost constant from 250 K to 50 K, indicating a gradual phase transition from the inverse triangular phase to the helical phase from 300 K to 250 K.²⁵ Below 250 K, a glassy ferromagnetic phase appears and co-exists with the helical phase at 50 K.²⁶ On the other hand, the magnetizations of $[\text{Mn}_3\text{Sn}(2.4)/\text{Cr}(0.15)]_{30}$ and MS50Cr10 both increase gradually from 300 K to 50 K and there is no inflection point, suggesting the absence phase transition and the inverse triangular spin structure

is maintained down to 50 K. In contrast, the magnetization of $[\text{Mn}_3\text{Sn}(2.4)/\text{Cr}(0.6)]_{30}$ increases dramatically at around 210 K and reaches almost 9 times of that at 300 K when the temperature reaches 50 K. This is presumably caused by the transition from AFM to ferromagnetic or glassy ferromagnetic phase below 210 K, though further studies are required to determine the exact magnetic structure.

Next, we turn to the electrical transport properties. Figure 3(a) shows the schematic diagram of electrical measurements, and the Hall measurement results for the aforementioned four samples are given in Fig. 3(b). In general, the Hall resistivity of Mn_3Sn has three main contributions and can be described as

$$\rho_{xy} = R_0 B + R_s \mu_0 M + \rho_{xy}^{AF}, \quad (2)$$

where M is the magnetization, R_0 (R_s) is the ordinary (anomalous) Hall coefficient (both are positive), B is the applied field, and μ_0 is the magnetic permeability.²⁷⁾ The last term, ρ_{xy}^{AF} , originates from the inverse triangular spin structure. As can be seen from Fig. 3(b), all the samples exhibit a negative AHE at 300 K, a hallmark of non-collinear AFM.^{3,4,26)} The zero-field ρ_{xy}^{AF} for Mn_3Sn at 300 K is about $-2.27 \mu\Omega \text{ cm}$, comparable with or larger than the reported values for polycrystalline films.^{16,17,24)} When T decreases to 250 K, the negative AHE decreases dramatically while a small positive component appears, indicating the transition from the AFM phase to the co-existence of helical and FM phases. This transition in AHE coincides with the transition observed in the M - H and M - T curves. When the temperature decreases further to 200 K, the negative component disappears and only a small positive component remains. This means that only the helical and FM phases exist in Mn_3Sn at 200 K. At 50 K, the AHE is vanishingly small due to the dominance of the spin glass phase.

In a sharp contrast, the temperature-dependence of AHE in $[\text{Mn}_3\text{Sn}(2.4)/\text{Cr}(0.15)]_{30}$ and $[\text{Mn}_3\text{Sn}(2.4)/\text{Cr}(0.6)]_{30}$ shows an opposite trend. In both samples, ρ_{xy}^{AF} increases monotonically with decreasing temperature. In $[\text{Mn}_3\text{Sn}(2.4)/\text{Cr}(0.15)]_{30}$, ρ_{xy}^{AF} at 300 K is $3.35 \mu\Omega \text{ cm}$ (hereafter we omit the negative sign), but it increases to $5.66 \mu\Omega \text{ cm}$ at 50 K, almost doubled from its room temperature value. Moreover, its room temperature value is also 47.6% higher than that of Mn_3Sn with almost the same thickness. On the other hand, ρ_{xy}^{AF} of $[\text{Mn}_3\text{Sn}(2.4)/\text{Cr}(0.6)]_{30}$ increases from $1.48 \mu\Omega \text{ cm}$ at 300 K to $2.52 \mu\Omega \text{ cm}$ at 50 K, which changes by 70%, albeit the absolute value is

much smaller than that of $[\text{Mn}_3\text{Sn}(2.4)/\text{Cr}(0.15)]_{30}$. In contrast, ρ_{xy}^{AF} of MS50Cr10 increases from $3.02 \mu\Omega \text{ cm}$ at 300 K to $3.8 \mu\Omega \text{ cm}$ at 200 K and then decreases to $2.42 \mu\Omega \text{ cm}$ at 50 K. In addition to these four samples, we have also varied the Cr thickness in the multilayer samples and sputtering power of the co-sputtered samples systematically. The temperature-dependence of ρ_{xy}^{AF} for all the samples are summarized in Fig. 3(c). The general trends are summarized as follows. In the case of $[\text{Mn}_3\text{Sn}(t_1)/\text{Cr}(t_2)]_{30}$ multilayers, when t_1 is fixed at 2.4 nm, t_2 in the range of 0.13 – 0.3 nm results in a significant enhancement of AHE throughout the temperature range investigated, *i.e.*, 50 – 300 K, as compared to Mn_3Sn . In fact, ρ_{xy}^{AF} for $[\text{Mn}_3\text{Sn}(2.4)/\text{Cr}(0.6)]_{30}$ keeps increasing slowly down to 10 K. When t_2 is fixed at 0.15 nm, a reduction of t_1 from 2.4 nm to 2 nm results in a non-monotonic temperature-dependence of AHE similar to that of co-sputtered samples, and a further decrease of t_1 to 1 nm leads to a vanishingly small AHE. On the other hand, for co-sputtered samples, when the sputtering power for Mn_3Sn is fixed at 50 W, the samples deposited at a Cr sputtering power of 10 and 30 W show a similar non-monotonic temperature-dependence of AHE, though ρ_{xy}^{AF} for the sample deposited at 10 W is much larger than that of the sample deposited at 30 W, $3.02 \mu\Omega \text{ cm}$ versus $1.79 \mu\Omega \text{ cm}$, at 300 K. These results suggest that there is a difference between the co-sputtered and multilayer samples even though the equivalent Cr composition is almost the same. The multilayer samples are presumably comprised of alternative layers of heavily doped and lightly or non-doped Mn_3Sn . The heavily doped region helps to stabilize the AFM phase at low temperature and the lightly doped region leads to an enhancement of AHE. Figure 3(d) shows the temperature-dependence of zero-field anomalous Hall conductivity (AHC), $\sigma_{xy} = \frac{-\rho_{xy}}{\rho_{xx}^2}$, where ρ_{xx} is the longitudinal resistivity at $H = 0$. At 300 K, σ_{xy} of $[\text{Mn}_3\text{Sn}(2.4)/\text{Cr}(0.15)]_{30}$, $[\text{Mn}_3\text{Sn}(2.4)/\text{Cr}(0.6)]_{30}$ and MS50Cr10 are $57.8 \Omega^{-1} \text{ cm}^{-1}$, $52.6 \Omega^{-1} \text{ cm}^{-1}$ and $41.6 \Omega^{-1} \text{ cm}^{-1}$, respectively. When the temperature decreases to 50 K, it reaches $184.8 \Omega^{-1} \text{ cm}^{-1}$, $149.9 \Omega^{-1} \text{ cm}^{-1}$ and $109.2 \Omega^{-1} \text{ cm}^{-1}$, respectively. As a comparison, σ_{xy} for Mn_3Sn is $39.5 \Omega^{-1} \text{ cm}^{-1}$ at 300 K and nearly 0 at 50 K. It is apparent that Cr-doping significantly enhances AHC, especially at low temperature. In addition to the large AHE, we have also observed large negative magnetoresistance (NMR) with $H//I$ in Cr-doped samples at low temperature (Figure S3 in supplementary data), around -0.15% for $[\text{Mn}_3\text{Sn}(2.4)/\text{Cr}(0.15)]_{30}$ at 50 K. The NMR, which is due to chiral anomaly,^{11,27} is reported to be inversely proportional to the energy spacing between the Weyl nodes and Fermi

level.²⁷⁾ Therefore, both the AHE and NMR results can be accounted for by the doping-induced narrowing of energy spacing between the Weyl nodes and Fermi level.

In summary, the Cr doping effect in Mn_3Sn polycrystalline films has been investigated. Both uniform and modulation doping with low Cr concentration do not cause notable changes to structural and magnetic properties of Mn_3Sn , but it significantly enhances the anomalous Hall effect, and the enhancement is particularly significant for modulation-doped samples at low temperature with the magnitude much larger than that of its bulk counterpart. The enhancement is presumably caused by the change of Fermi level induced by Cr doping. Compared to uniform doping, modulation doping has the advantage that the dopant distribution is more regular in the thickness direction which helps to suppress doping-induced disorder, as manifested in the large enhancement of AHE, especially at low temperature. Our results may open new opportunities for both device applications and fundamental studies of Mn_3Sn at low temperature.

Acknowledgments

This work is supported by Ministry of Education, Singapore under its Tier 2 Grants (grant no. MOE2017-T2-2-011 and MOE2018-T2-1-076). We thank Profs Shufeng Zhang, Ryotaro Arita, and Jingsheng Chen for helpful discussions.

References

- 1) Hua Chen, Qian Niu, and A. H MacDonalD, *Physical Review Letters* **112**, 017205 (2014).
- 2) J. Kübler and C. Felser, *EPL (Europhysics Letters)* **108**, 67001 (2014).
- 3) Satoru Nakatsuji, Naoki Kiyohara, and Tomoya Higo, *Nature* **527**, 212 (2015).
- 4) Ajaya K. Nayak, Julia Erika Fischer, Yan Sun, Binghai Yan, Julie Karel, Alexander C. Komarek, Chandra Shekhar, Nitesh Kumar, Walter Schnelle, Jürgen Kübler, Claudia Felser, and Stuart S. P. Parkin, *Science Advances* **2**, e1501870 (2016).
- 5) Muhammad Ikhlas, Takahiro Tomita, Takashi Koretsune, Michi-To Suzuki, Daisuke Nishio-Hamane, Ryotaro Arita, Yoshichika Otani, and Satoru Nakatsuji, *Nature Physics* **13**, 1085 (2017).
- 6) Libor Šmejkal, Yuriy Mokrousov, Binghai Yan, and Allan H. MacDonalD, *Nature Physics* **14**, 242 (2018).
- 7) Tomoya Higo, Huiyuan Man, Daniel B. Gopman, Liang Wu, Takashi Koretsune, Olaf M. J. van 't Erve, Yury P. Kabanov, Dylan Rees, Yufan Li, Michi-To Suzuki, Shreyas Patankar, Muhammad Ikhlas, C. L. Chien, Ryotaro Arita, Robert D. Shull, Joseph Orenstein, and Satoru Nakatsuji, *Nature Photonics* **12**, 73 (2018).
- 8) Z. Q. Liu, H. Chen, J. M. Wang, J. H. Liu, K. Wang, Z. X. Feng, H. Yan, X. R. Wang, C. B. Jiang, J. M. D. Coey, and A. H. MacDonalD, *Nature Electronics* **1**, 172 (2018).
- 9) Hanshen Tsai, Tomoya Higo, Kouta Kondou, Takuya Nomoto, Akito Sakai, Ayuko Kobayashi, Takafumi Nakano, Kay Yakushiji, Ryotaro Arita, Shinji Miwa, Yoshichika Otani, and Satoru Nakatsuji, *Nature* **580**, 608 (2020).
- 10) Yutaro Takeuchi, Yuta Yamane, Ju-Young Yoon, Ryuichi Itoh, Butsurin Jinnai, Shun Kanai, Jun'ichi Ieda, Shunsuke Fukami, and Hideo Ohno, *Nature Materials* (2021).
- 11) K. Kuroda, T. Tomita, M. T. Suzuki, C. Bareille, A. A Nugroho, P. Goswami, M. Ochi, M. Ikhlas, M. Nakayama, S. Akebi, R. Noguchi, R. Ishii, N. Inami, K. Ono, H. Kumigashira, A. Varykhalov, T. Muro, T. Koretsune, R. Arita, S. Shin, Takeshi Kondo, and S. Nakatsuji, *Nature Materials* **16**, 1090 (2017).
- 12) Hao Yang, Yan Sun, Yang Zhang, Wu-Jun Shi, Stuart S. P. Parkin, and Binghai Yan, *New Journal of Physics* **19**, 015008 (2017).
- 13) M. T. Suzuki, T. Koretsune, M. Ochi, and R. Arita, *Physical Review B* **95**, 094406 (2017).

- 14) Jakub Železný, Yang Zhang, Claudia Felser, and Binghai Yan, *Physical Review Letters* **119**, 187204 (2017).
- 15) Motoi Kimata, Hua Chen, Kouta Kondou, Satoshi Sugimoto, Prasanta K. Muduli, Muhammad Ikhlas, Yasutomo Omori, Takahiro Tomita, Allan H. MacDonald, Satoru Nakatsuji, and Yoshichika Otani, *Nature* **565**, 627 (2019).
- 16) Tomoya Higo, Danru Qu, Yufan Li, C. L. Chien, Yoshichika Otani, and Satoru Nakatsuji, *Applied Physics Letters* **113**, 202402 (2018).
- 17) Tomoki Ikeda, Masakiyo Tsunoda, Mikihiro Oogane, Seungjun Oh, Tadashi Morita, and Yasuo Ando, *Applied Physics Letters* **113**, 222405 (2018).
- 18) Tomoki Ikeda, Masakiyo Tsunoda, Mikihiro Oogane, Seungjun Oh, Tadashi Morita, and Yasuo Ando, *AIP Advances* **10**, 015310 (2020).
- 19) Yunfeng You, Xianzhe Chen, Xiaofeng Zhou, Youdi Gu, Ruiqi Zhang, Feng Pan, and Cheng Song, *Advanced Electronic Materials* **5**, 1800818 (2019).
- 20) A. Markou, J. M. Taylor, A. Kalache, P. Werner, S. S. P. Parkin, and C. Felser, *Physical Review Materials* **2**, 051001 (2018).
- 21) Juyoung Yoon, Yutaro Takeuchi, Ryuichi Itoh, Shun Kanai, Shunsuke Fukami, and Hideo Ohno, *Applied Physics Express* **13**, 013001 (2019).
- 22) Ju-Young Yoon, Yutaro Takeuchi, Samik DuttaGupta, Yuta Yamane, Shun Kanai, Jun'ichi Ieda, Hideo Ohno, and Shunsuke Fukami, *AIP Advances* **11**, 065318 (2021).
- 23) Xiaoning Wang, Zexin Feng, Peixin Qin, Han Yan, Xiaorong Zhou, Huixin Guo, Zhaoguogang Leng, Weiqi Chen, Qiannan Jia, Zexiang Hu, Haojiang Wu, Xin Zhang, Chengbao Jiang, and Zhiqi Liu, *Acta Materialia* **181**, 537 (2019).
- 24) Zhongping Zhao, Qi Guo, Fenghua Chen, Kewei Zhang, and Yong Jiang, *Physica B: Condensed Matter* **604**, 412692 (2021).
- 25) N. H. Sung, F. Ronning, J. D. Thompson, and E. D. Bauer, *Applied Physics Letters* **112**, 132406 (2018).
- 26) James M. Taylor, Anastasios Markou, Edouard Lesne, Pranava Keerthi Sivakumar, Chen Luo, Florin Radu, Peter Werner, Claudia Felser, and Stuart S. P. Parkin, *Physical Review B* **101**, 094404 (2020).

- 27) Durga Khadka, T. R. Thapaliya, Sebastian Hurtado Parra, Xingyue Han, Jiajia Wen, Ryan F. Need, Pravin Khanal, Weigang Wang, Jiadong Zang, James M. Kikkawa, Liang Wu, and S. X. Huang, *Science Advances* **6**, eabc1977 (2020).

Figure Captions

Fig. 1. XRD spectra for Mn_3Sn (72), $[\text{Mn}_3\text{Sn}(2.4)/\text{Cr}(t_2)]_{30}$ and co-sputtered samples MS50Cr30 and MS50Cr10.

Fig. 2. M - H curves measured at 300 K with the field applied out-of-plane (red solid-line), in-plane 0° (green dotted-line), in-plane 45° (purple dashed-line) and in-plane 90° (black dash dotted-line) for (a) Mn_3Sn , (b) $[\text{Mn}_3\text{Sn}(2.4)/\text{Cr}(0.15)]_{30}$, (c) $[\text{Mn}_3\text{Sn}(2.4)/\text{Cr}(0.6)]_{30}$ and (d) MS50Cr10. (e) M - T curves from 50 K to 300 K under a 200 Oe out-of-plane magnetic field.

Fig. 3. (a) Schematic of Hall bar and electrical transport measurement. (b) Magnetic field-dependence of anomalous Hall resistivity for Mn_3Sn , $[\text{Mn}_3\text{Sn}(2.4)/\text{Cr}(t_2)]_{30}$ and MS50Cr10 at different temperatures. (c) Temperature-dependence of zero-field Hall resistivity for different samples. (d) Temperature-dependence of zero-field AHC for Mn_3Sn , $[\text{Mn}_3\text{Sn}(2.4)/\text{Cr}(t_2)]_{30}$ and MS50Cr10.

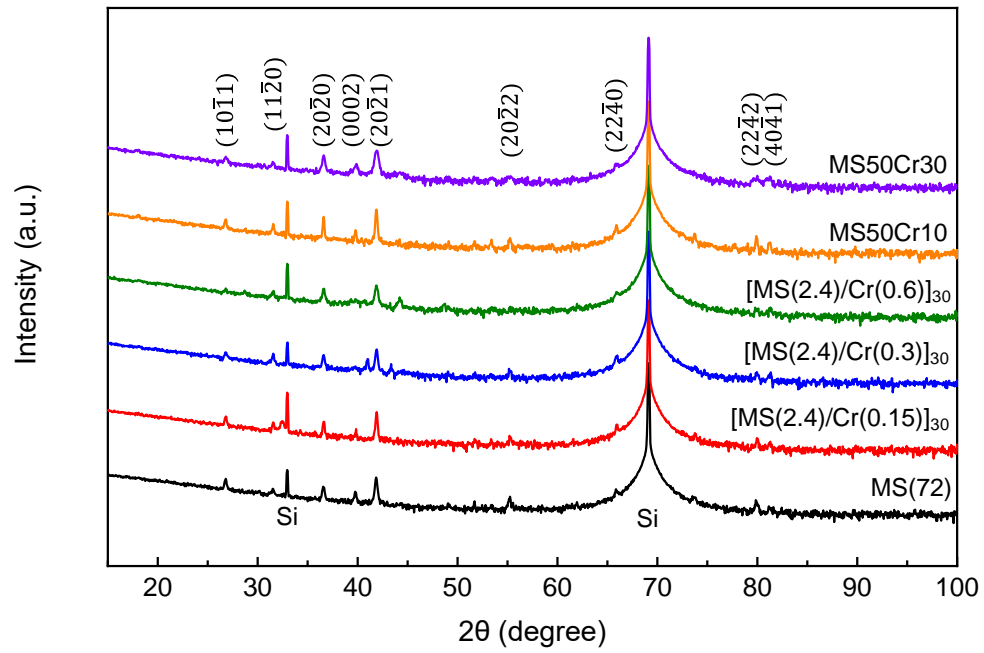


Figure 1

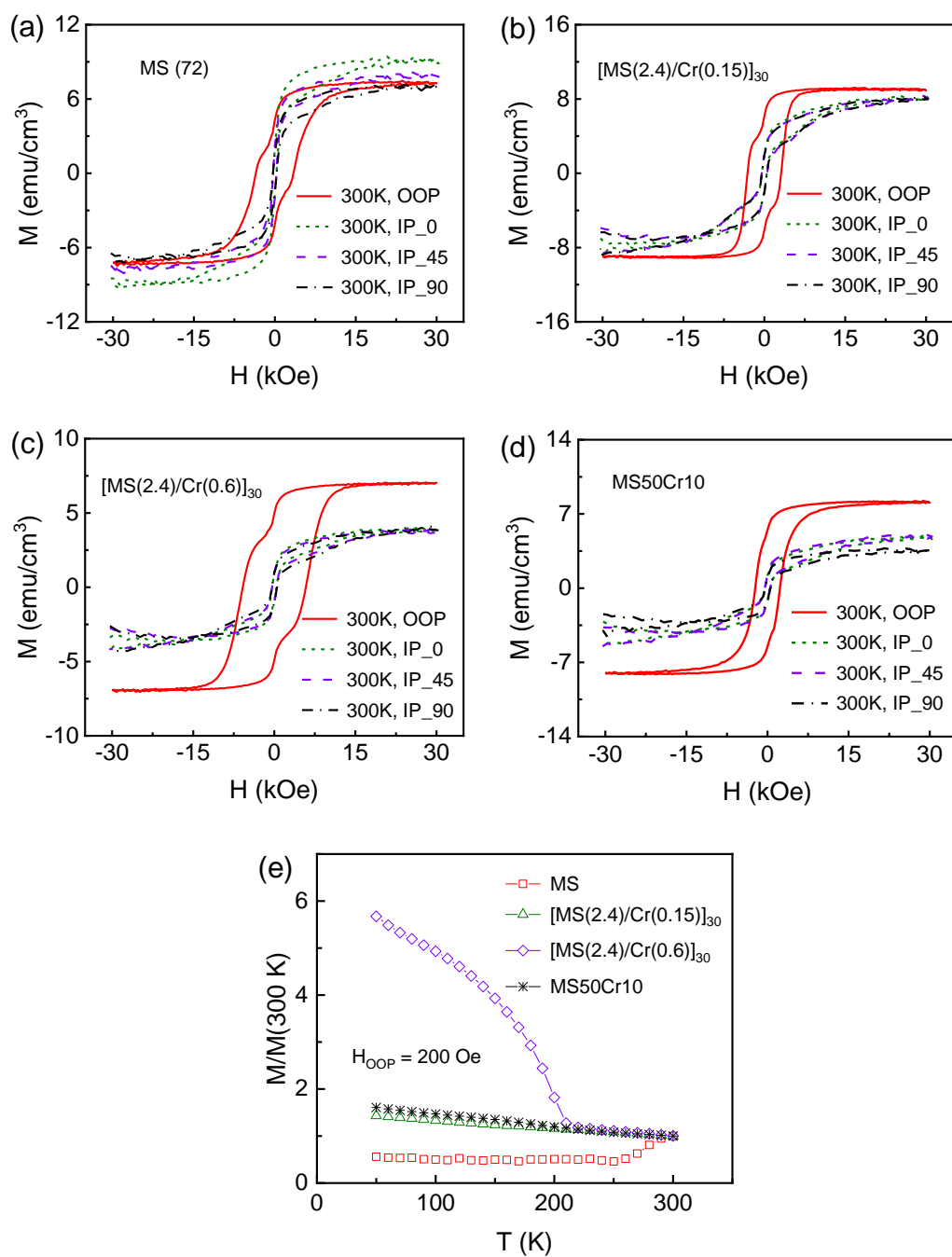


Figure 2

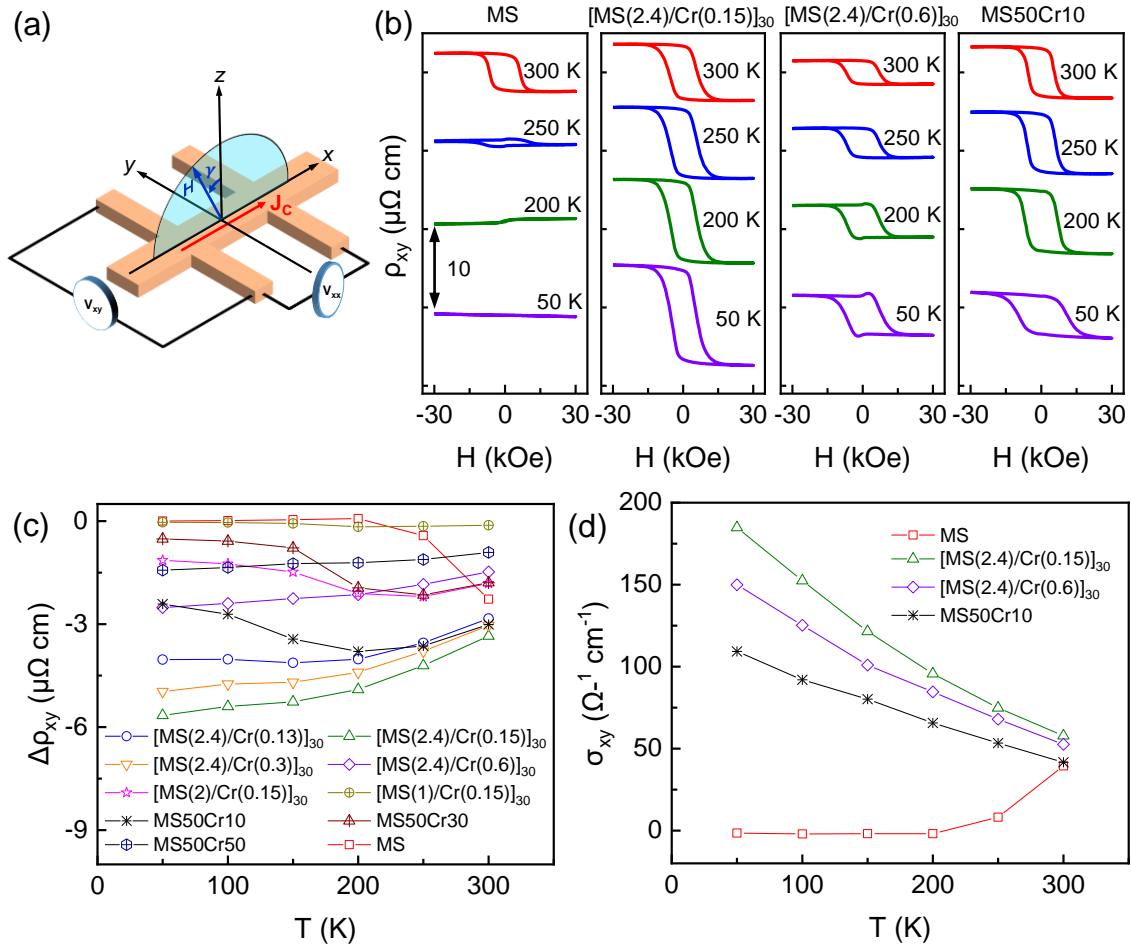


Figure 3